Analytical and Experimental Studies of the Dynamics of Variable Topology Systems

Josep M. Font-Llagunes [1], József Kövecses [2]

[1] Department of Mechanical Engineering, Universitat Politècnica de Catalunya
Diagonal 647, 08028 Barcelona, Catalunya, Spain
josep.m.font@upc.edu

[2] Department of Mechanical Engineering and Centre for Intelligent Machines, McGill University
817 Sherbrooke St. West, H3A 2K6 Montréal, Québec, Canada
jozsef.kovecses@mcgill.ca

Abstract—*Mechanical systems with time-varying topology appear frequently in various applications. The nature of topology transition is a key characteristic in the performance of such systems. In this paper, a concept to decouple kinematic and kinetic quantities at the time of topology transition is used. This approach relies on the use of impulsive bilateral constraints and it is a useful tool for the analysis of energy redistribution and velocity change when these constraints are suddenly established. Based on this concept, two examples of systems with time-varying topology are analyzed: a bipedal walking system and a dual-pantograph robotic prototype interacting with a stiff environment. Detailed numerical and experimental analysis to gain insight into the dynamics and energetics of topology transitions is presented.*

Index Terms—*Kinematics and Dynamics of Reconfiguration, Reconfigurable Robots, Various Topology Modeling.*

1. Introduction

Variable topology mechanical systems are present in various fields of research such as robotics, biomechanics or mechanism science. The dynamic analysis of such systems depends on the time-varying nature of the connections between the elements of the system and the environment. This complicates the analysis because in most cases a different dynamic model must be developed for each constraint condition.

Different situations can be found depending on how these connections are established. For example, one possibility is that the number of degrees of freedom of the system decreases due to the development of certain "new" connections with other objects or the environment. This is the case of the grasping/capturing of a moving payload, or also the interaction of two robotic mechanisms. The effect of mass capture on flexible multibody systems was studied in [1] and [2].

A second possibility appears when at the same time of establishing new connections, other previous constraints become passive. In such a case, the number of degrees of freedom may vary or stay the same depending on the specific constraints. An example for this situation can be found in the analysis of (active/passive) dynamic walking machines [3]. In those systems, the heel strike event represents a sudden change of topology where some constraints are imposed on the foot that makes contact with the ground, and other are released from the foot that lifts up [4], [5].

Discontinuous constraints have been a known concept in analytical mechanics [6], [7], [8]. As discussed before, two particular cases of such discontinuous constraint configurations can be the sudden removal and the sudden addition of constraints. The sudden removal of constraints alone does not instantaneously change the energy and momentum distribution of the system unless other impulsive forces (applied or constraint forces) are present. The sudden addition of constraints does cause instantaneous changes. Therefore, the truly critical event during the motion of variable topology systems is when physical connections are established. Such an event can be characterized by inert constraints which are a class of bilateral impulsive constraints [6], [7], [8].

This work focuses on this event and particularly on the effects of the system state (configuration and velocities) on various dynamic aspects of the transition. The dynamic analysis conducted in this work is based on an analytical approach that allows a complete decomposition of the dynamic equations and the kinetic energy to two subspaces of the tangent space of the system, i.e., the spaces of constrained and admissible motions [9]. It will be shown that this approach is useful to better understand topology-varying systems and get insight into their dynamic behaviour during contact.

Two situations that can be characterized by means of inert constraints are studied in this paper. We focus first on the heel strike event of bipedal locomotion. This is a relevant event because it represents the main cause of energy consumption during the gait cycle [5]. Furthermore, it plays an important role to guarantee the cyclic stability of the motion. Different dynamic aspects of the heel strike are analyzed, paying special attention on the energy redistribution during topology transition. The magnitude of the contact impulses developed on the foot are also calculated for different configurations and design parameters of the system.

The second example studied in the paper is the case of a robotic multibody system that makes contact with a stiff environment. An experimental testbed consisting of two dual-pantograph devices is used for that purpose. By means of it, detailed experimental analysis is carried out to illustrate different concepts introduced in this work.

2. DYNAMICS FORMULATION

Let us consider that the configuration of the system can be described by n generalized coordinates that are represented by the $n \times 1$ dimensional array $\mathbf{q}$. The time derivatives of these coordinates $\dot{\mathbf{q}}$ give a possible set of generalized velocities of the system. We will consider that $(\mathbf{q},\ \dot{\mathbf{q}})$ represents a minimum set of generalized coordinates and velocities with respect to the continuous constraints imposed on the system. In this paper, we will primarily consider systems where the kinetic energy can be expressed as a quadratic function of the generalized velocities

$$T = \frac{1}{2}\dot{\mathbf{q}}^T \mathbf{M} \dot{\mathbf{q}}, \tag{1}$$

where $\mathbf{M}(\mathbf{q})$ is the $n \times n$ mass matrix of the system. The dynamic equations of motion of such a multibody system can generally be written as

$$\mathbf{M}\ddot{\mathbf{q}} + \mathbf{c} + \mathbf{u} = \mathbf{f}_A + \mathbf{f}_R + \mathbf{f}_N, \tag{2}$$

where $\mathbf{c}(\mathbf{q}, \dot{\mathbf{q}})$ represents the Coriolis and centrifugal effects, $\mathbf{u}(\mathbf{q})$ is the negative of the generalized conservative forces, $\mathbf{f}_A$ and $\mathbf{f}_R$ are the generalized applied and constraint forces respectively, and $\mathbf{f}_N$ represents generalized non-ideal forces that may arise due to the non-ideal realization of constraints.

Let us consider that t_i represents the time point when certain constraints are suddenly established and, as a result, the topology of the system changes. This sudden addition/imposition of physical restrictions on the system motion can be modeled by means of inert constraints [6], [8]. The event of topology transition takes place in the $[t_i^-,\ t_i^+]$ interval, where t_i^- and t_i^+ represent the so-called pre- and post-event instants. The duration of this interval can usually be considered very short on the characteristic time scale of the finite (continuous) motion of the system. Therefore, the configuration of the system is assumed to remain unchanged during $[t_i^-,\ t_i^+]$, and the event of topology change is analyzed as an impulsive motion event. Inert constraints can normally be written as

$$\mathbf{A}\dot{\mathbf{q}}^+ = \mathbf{0}, \tag{3}$$

where $\dot{\mathbf{q}}^+$ stands for $\dot{\mathbf{q}}$ at t_i^+, and $\mathbf{A}$ is the $m \times n$ dimensional constraint Jacobian. These can generally be considered as impulsive non-holonomic constraints [6], [8], and they represent the required topology at t_i^+ at the velocity level.

Two typical situations may arise depending on whether the new constraints persist for a finite period of time or they represent only an instantaneous situation. One example for the first situation appears in bipedal locomotion when the swing leg makes contact with the ground at heel strike. This will be analyzed in Section 4. For the second situation, an example can be the general consideration of low velocity impact between two bodies when the duration of the impact "looks" instantaneous on the characteristic time scale determined by the finite motion of the system. Such impact can be divided to two phases (namely, compression and restitution phases) and the system configuration is usually assumed constant during the whole event. The compression phase can be modeled with constraints of the form of Eq. (3), where $\dot{\mathbf{q}}^+$ represents the generalized velocities at the end of compression when the relative normal velocity of the contact points is zero. This case will be experimentally analyzed in Section 6.

2.1. Dynamics Decomposition

The tangent space of the dynamic system can be seen as an n dimensional linear space interpreted for each configuration [10], [11]. Since the configuration of the system can be assumed constant in $[t_i^-,\ t_i^+]$, a single interpretation of this linear space may be used for both t_i^- and t_i^+. The inert constraints and their Jacobian $\mathbf{A}$ can be employed to decompose this tangent space to the space of constrained motion (SCM) and space of admissible motion (SAM) [9].

The above two subspaces can be defined so that they are orthogonal to each other with respect to the mass metric of the tangent space [9], [12]. In this case, any impulsive event characterized by ideal inert constraints of the form of Eq. (3) will influence quantities in the SCM leaving the SAM unaffected. However, non-ideal effects, such as friction, can couple the two subspaces and develop an influence on the admissible motion dynamics too. The decomposition to the two subspaces can be accomplished using two projection operators [9], [12]. The projectors associated with the SCM and the SAM can be respectively written as

$$\mathbf{P}_c = \mathbf{M}^{-1}\mathbf{A}^T \left(\mathbf{A}\mathbf{M}^{-1}\mathbf{A}^T\right)^{-1} \mathbf{A}, \tag{4}$$

$$\mathbf{P}_a = \mathbf{I} - \mathbf{P}_c = \mathbf{I} - \mathbf{M}^{-1}\mathbf{A}^T \left(\mathbf{A}\mathbf{M}^{-1}\mathbf{A}^T\right)^{-1} \mathbf{A}, \tag{5}$$

where $\mathbf{I}$ is the $n \times n$ identity matrix. The mathematical derivation for these projectors can be found in [11], [9]. It can be seen that the projectors above satisfy that $\mathbf{P}_a^T \mathbf{M} \mathbf{P}_c = \mathbf{0}$, where $\mathbf{0}$ denotes the $n \times n$ zero matrix, which shows the orthogonality of $\mathbf{P}_c$ and $\mathbf{P}_a$ with respect to the mass matrix.

Using the above operators, the generalized velocities of the system can be decomposed as

$$\dot{\mathbf{q}} = \mathbf{v}_c + \mathbf{v}_a = \mathbf{P}_c\dot{\mathbf{q}} + \mathbf{P}_a\dot{\mathbf{q}}, \tag{6}$$

which represent the two components associated with the subspaces. It is interesting to note that $\mathbf{v}_c = \mathbf{P}_c\dot{\mathbf{q}}$ and $\mathbf{v}_a = \mathbf{P}_a\dot{\mathbf{q}}$ are generally non-holonomic components. Based on Eq. (6), it can be seen that the kinetic energy can be decomposed as

$$T = T_c + T_a = \frac{1}{2}\mathbf{v}_c^T \mathbf{M} \mathbf{v}_c + \frac{1}{2}\mathbf{v}_a^T \mathbf{M} \mathbf{v}_a, \tag{7}$$

which represents a complete decoupling of T [9], [12]. To obtain Eq. (7) it was used that $\mathbf{v}_a^T \mathbf{M} \mathbf{v}_c = 0$, which is a direct consequence of the orthogonality of the projectors with respect to $\mathbf{M}$. Any vector of generalized forces or generalized impulses can also be decomposed using the transpose of $\mathbf{P}_c$ and $\mathbf{P}_a$ as

$$\mathbf{f} = \mathbf{f}_c + \mathbf{f}_a = \mathbf{P}_c^T\mathbf{f} + \mathbf{P}_a^T\mathbf{f}, \tag{8}$$

and

$$\bar{\mathbf{f}} = \bar{\mathbf{f}}_c + \bar{\mathbf{f}}_a = \mathbf{P}_c^T\bar{\mathbf{f}} + \mathbf{P}_a^T\bar{\mathbf{f}}, \tag{9}$$

where $\bar{\mathbf{f}}$ is the impulse of $\mathbf{f}$. It is also possible to show that $\mathbf{f}_a^T \mathbf{M}^{-1} \mathbf{f}_c = 0$ and $\bar{\mathbf{f}}_a^T \mathbf{M}^{-1} \bar{\mathbf{f}}_c = 0$ hold for the general case.

3. DYNAMICS AND ENERGETICS OF TOPOLOGY CHANGE

The dynamics of the instantaneous imposition of constraints can be characterized by impulse-momentum level dynamic equations. Based on Eqs. (1) and (2), these can be obtained in a general form as [13], [8]

$$\left[\frac{\partial T}{\partial \dot{\mathbf{q}}}\right]_{-}^{+} = \mathbf{M}\left(\dot{\mathbf{q}}^{+} - \dot{\mathbf{q}}^{-}\right) = \bar{\mathbf{f}}_A + \bar{\mathbf{f}}_R + \bar{\mathbf{f}}_N, \qquad (10)$$

where "$-$" and "$+$" denote the pre- and post-event instants, $\bar{\mathbf{f}}_A$, $\bar{\mathbf{f}}_R$ and $\bar{\mathbf{f}}_N$ are the impulses of the generalized applied, constraint, and non-ideal forces, and $[\partial T/\partial \dot{\mathbf{q}}]_{-}^{+} = -\bar{\mathbf{f}}_I$ is the negative of the impulse of the generalized inertial forces according to principle of virtual work. If the applied forces are non-impulsive, then $\bar{\mathbf{f}}_A = \mathbf{0}$. This is the case we will study in more detail to gain insight into the effect of inert constraints representing the topology change. As it was discussed earlier, the only impulsive constraint forces are associated with the inert constraints. For now we will also assume that these constraints are realized in an ideal way, i.e., $\bar{\mathbf{f}}_N = \mathbf{0}$. The impulsive constraint forces responsible for the topology change can be written as

$$\bar{\mathbf{f}}_R = \mathbf{A}^T \bar{\boldsymbol{\lambda}}, \qquad (11)$$

where $\bar{\boldsymbol{\lambda}}$ represents the impulse of the contact forces developed during this event and $\mathbf{A}$ is the Jacobian in Eq. (3).

Based on the decompositions introduced in Section 2.1, the impulsive dynamic equations provided in Eq. (10) can also be decoupled. The dynamic equations associated with the SCM and the SAM can be respectively expressed as

$$\left[\frac{\partial T_c}{\partial \mathbf{v}_c}\right]_{-}^{+} = \mathbf{M}\left(\mathbf{v}_c^{+} - \mathbf{v}_c^{-}\right) = \mathbf{A}^T \bar{\boldsymbol{\lambda}}, \qquad (12)$$

$$\left[\frac{\partial T_a}{\partial \mathbf{v}_a}\right]_{-}^{+} = \mathbf{M}\left(\mathbf{v}_a^{+} - \mathbf{v}_a^{-}\right) = \mathbf{0}. \qquad (13)$$

Eqs. (12) and (13) provide useful information to analyze the dynamics of topology transition for the case of ideal constraints. First of all, it can be seen that constraint impulses $\bar{\mathbf{f}}_R$ are fully projected to the space of constrained motion. Based on Eq. (13) and taking into account that $\mathbf{M}$ is invertible, it can be easily seen that $\mathbf{v}_a^{+} = \mathbf{v}_a^{-}$. Hence, based on Eq. (7) one can conclude that the kinetic energy of the SAM is the same before and after the topology transition, $T_a^{+} = T_a^{-}$.

Also, based on Eqs. (12), (3) and (6) it can be concluded that $\mathbf{v}_c^{+} = \mathbf{0}$. This implies that no matter how much kinetic energy is contained in the SCM at the pre-event time, this will be completely "lost" during topology transition since $T_c^{+} = 0$.

The last considerations can be useful to gain insight into energetic aspects of the sudden change of topology. During interval $[t_i^{-},\ t_i^{+}]$, the constraint impulses on the system will change only T_c while leaving T_a unaffected. The kinetic energy decomposition at pre-impact time, $T^{-} = T_c^{-} + T_a^{-}$, provides the energetic balance of the whole event since T_c^{-} is the part of the energy that will be lost and T_a^{-} will not be modified and will remain in the system after the transition. Therefore, at time instant t_i^{+} we have that $T^{+} = T_a^{-}$ which is less or equal to T^{-} according to Carnot's theorem [6].

Based on Eq. (12) and the fact that $\mathbf{v}_c^{+} = \mathbf{0}$, we obtain that

$$-\mathbf{M}\mathbf{v}_c^{-} = \mathbf{A}^T \bar{\boldsymbol{\lambda}}. \qquad (14)$$

Also, considering that $\mathbf{v}_c^{+} = \mathbf{0}$, we can solve for the post-event generalized velocities $\dot{\mathbf{q}}^{+}$ as

$$\dot{\mathbf{q}}^{+} = \mathbf{v}_a^{+} = \mathbf{v}_a^{-} = \mathbf{P}_a \dot{\mathbf{q}}^{-}. \qquad (15)$$

The solution for the constraint impulse $\bar{\boldsymbol{\lambda}}$ can be found based on Eqs. (6) and (14). It yields the following expression

$$\bar{\boldsymbol{\lambda}} = -\left(\mathbf{A}\mathbf{M}^{-1}\mathbf{A}^T\right)^{-1} \mathbf{A}\mathbf{v}_c^{-}. \qquad (16)$$

Finally, based on Eqs. (6), (7) and (14), and using that $\mathbf{v}_a^T \mathbf{M} \mathbf{v}_c = 0$, it is possible to write that

$$-(\dot{\mathbf{q}}^{-})^T \mathbf{M} \mathbf{v}_c^{-} = -2T_c^{-} = (\dot{\mathbf{q}}^{-})^T \mathbf{A}^T \bar{\boldsymbol{\lambda}}, \qquad (17)$$

which shows that for a given pre-event velocity, the impulse of the constraint forces is proportional to the pre-event T_c^{-}. This makes it possible to express an explicit relationship between the impulses generated by the topology change and the kinetic energy content that is lost in the event.

4. EXAMPLE 1: BIPEDAL LOCOMOTION

An interesting example of systems with time-varying topology are bipedal walking systems. The event that represents such change of topology is the heel strike, when constraints on the swing foot are suddenly established. The constraint configuration imposes that this foot stays in contact with the ground without slipping after heel strike, i.e., the velocity of the contact point P is zero at the post-event time. This is the desired situation in walking motion, which can be expressed by inert constraints of the form of Eq. (3) as $\mathbf{v}_P^{+} \equiv \mathbf{A}\dot{\mathbf{q}}^{+} = \mathbf{0}$. After this event, the swing foot changes its role and becomes the stance foot of the next step.

The other foot also undergoes a transition at heel strike. Two different situations may arise depending on whether this foot stays or not in contact with the ground after heel strike. If the foot stays in contact with the ground, then a finite double-support phase appears right after the heel strike where the system has less degrees of freedom than before. This is the case of human locomotion. The other possibility is that the pre-impact stance foot instantaneously lifts up after heel strike, then constraints on this foot are suddenly removed, and the total number of degrees of freedom of the system stays the same (although constraints have changed). This is the case of a number of dynamic walking systems both active or actuated.

We will analyze here the heel strike event of a compass walker with circular feet and an upper body (torso). This system is shown in Fig. 1. It consists of two identical legs of length l and mass m. The center of mass (COM) of each leg is at a distance b from the hip. The radius of the feet is R and the hip is modeled as a point mass m_H located at the revolute joint between the legs. The torso is included as

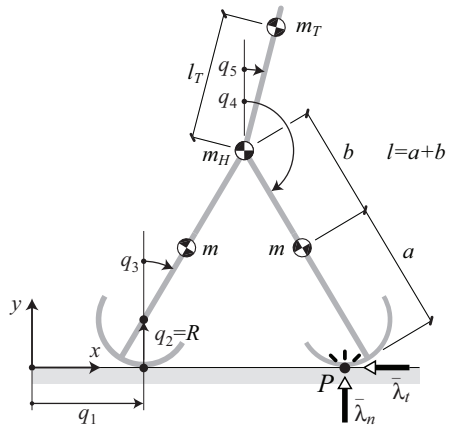

Fig. 1. Dynamic model of the compass walker with upper body

a third link that can rotate about the hip with mass m_T and the center of mass located at a distance l_T from the hip. The value of the fixed parameters is given in Table I. We define two dimensionless parameters which will be varied to investigate its dynamic effects. These are $\rho = \frac{R}{l}$, which establishes a relationship between the foot radius and the length of the leg, and $\mu = \frac{m_T}{2m}$, which accounts for the mass distribution between upper and lower body.

The configuration of this system can be described by the 5 generalized coordinates shown in Fig. 1. These define the 5×1 dimensional array $\mathbf{q}$. Coordinates q_1 and q_2 indicate the (x, y)-position of the center of the stance foot. Angles q_3, q_4 and q_5 indicate the absolute orientation of the stance leg, the swing leg and the upper body, respectively. The time derivatives of these coordinates define the vector of generalized velocities $\dot{\mathbf{q}}$.

For the system at hand, we obtained the mass matrix $\mathbf{M}$ and the Jacobian $\mathbf{A}$ associated with the constraints established at heel strike. Based on them, the projectors $\mathbf{P}_c$ and $\mathbf{P}_a$ were determined to calculate the kinetic energy decomposition and the impulses developed on the contact point $\bar{\boldsymbol{\lambda}} = [\bar{\lambda}_t\ \bar{\lambda}_n]^T$.

The dynamics analysis of topology change is based on the pre-impact velocities $\dot{\mathbf{q}}^-$. To obtain this vector the following assumptions were made for the pre-impact kinematics: (1) the stance foot rolls over the ground without slipping, $\dot{q}_1^- = R\dot{q}_3^-$ and $\dot{q}_2^- = 0$, (2) the upper body does not rotate with respect to the absolute inertial frame, $\dot{q}_5^- = 0$, and (3) both legs rotate with an angular velocity of 1 rad/s with respect to the absolute inertial frame, $\dot{q}_3^- = \dot{q}_4^- = 1$ rad/s. The previous values of $\dot{q}_3^-$ and $\dot{q}_4^-$ are typical for compass-gait walkers [14], [15].

TABLE I
PARAMETERS OF THE COMPASS-GAIT WALKER

Parameter	Value	Description
m_W	30 kg	Total mass of the walking system
m_H	10 kg	Mass of the hip
l	0.8 m	Length of the leg ($l = a + b$)
b	0.4 m	Position of the COM of the leg
l_T	0.4 m	Position of the COM of the torso

4.1. Effects of Lower Body Configuration and Feet Radius

In this section, we study the influence of one design parameter, radius R, and the angle θ between legs on two dynamic aspects of the heel strike transition: the energetic balance and the impulses developed on the foot. Note that angle $\theta = 2q_3$ at heel strike. We consider the following interval of possible angles: $\theta = [10°,\ 60°]$. As for the configuration of the upper body, we assume that it is placed perpendicular to the ground, i.e., $q_5 = 0°$. The effect of the foot radius design is analyzed considering the following values of ρ: 0, 0.25, and 0.5. The parameter representing the mass distribution is $\mu = 1$.

Figs. 2 and 3 represent, respectively, the kinetic energy decomposition at the pre-event time and the magnitude of impulses developed as a function of θ for the considered values of ρ. The pre-event energy decomposition is useful because it indicates the energy which will be lost during topology change (T_c^-) and the energy that will remain in the system (T_a^-).

Based on Fig. 2, it can be concluded that both the foot radius and the angle between legs have an important effect on the energy redistribution at heel strike. Since T_c^- is the energy that will be lost to establish the new constraint condition, it can be clearly seen that the larger the foot radius is, the lower the energetic losses are at heel strike. Also, for a given foot radius, a low interleg angle θ provides lower energetic losses. This can provide guidelines for design and gait synthesis to minimize the energy consumption of humanoid robots. It can be seen that a point-feet walker ($\rho = 0$) is clearly less efficient than a circular-feet walker ($\rho > 0$), which is in complete agreement with [16] and [17]. In Fig. 2 the curve for $\rho = 0$ does not cover all the range of angles because for $\theta > 43°$ the stance foot does not lift up from the ground after heel strike and, therefore, walking motion cannot be obtained.

Regarding the contact impulses $\bar{\lambda}_n$ (normal direction) and $\bar{\lambda}_t$ (tangential direction), Fig. 3 shows that both of them grow with θ and decrease with ρ. The point-feet walker ($\rho = 0$) is the one that yields higher impulses for a given θ (in both directions). As it was deduced from Eq. (17) the impulse vector $\bar{\boldsymbol{\lambda}}$ and T_c^- are related to each other, therefore, high contact impulses are obtained when T_c^- is also high. This is in agreement with the results shown in Figs. 2 and 3.

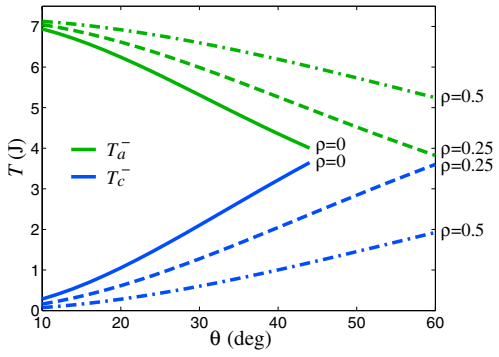

Fig. 2. Kinetic energy decomposition at t_i^- as a function of θ, ρ

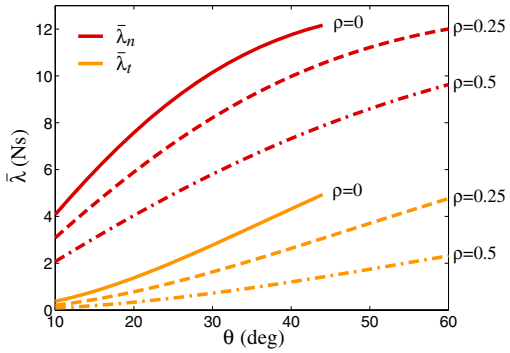

Fig. 3. Impulses developed at heel strike as a function of θ, ρ

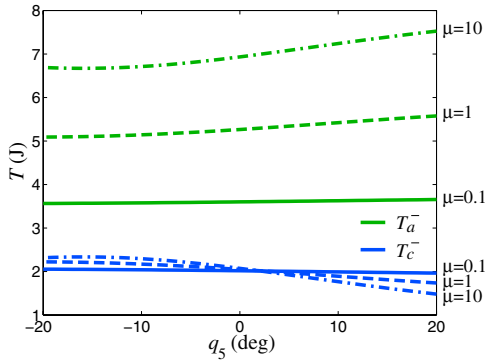

Fig. 4. Kinetic energy decomposition at t_i^- as a function of q_5, μ

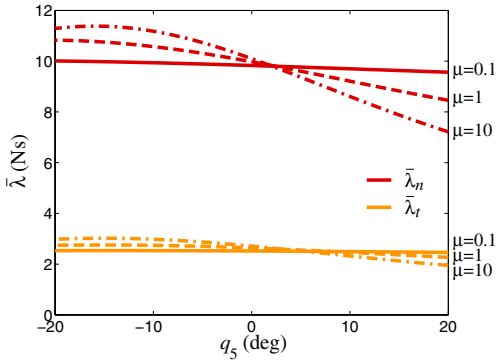

Fig. 5. Impulses developed at heel strike as a function of q_5, μ

4.2. Effects of Upper Body Configuration and Mass Distribution

In this section, we analyze how the upper body configuration and the walker mass distribution affect the dynamics of heel strike. For this purpose, we study impacts for a usual interleg angle $\theta = 40°$, and a fixed foot radius $R = 0.25\,l$. The influence of the configuration of the upper body is analyzed by varying angle q_5 within the range $[-20°,\ 20°]$. That is, configurations between upper body leaning backward aligned with the front leg ($q_5 = -20°$) and upper body leaning forward aligned with the rear leg ($q_5 = 20°$). As for the mass distribution, its effects are studied by considering the following values of μ: 0.1, 1, and 10.

Figs. 4 and 5 represent the kinetic energy decomposition at the pre-event time and the magnitude of the developed impulses as a function of q_5 for the considered values of μ. Several conclusions can be drawn from the results plotted in Fig. 4. First of all, it can be seen that a body posture with the torso leaning forward ($q_5 > 0°$) is better to reduce the energy loss (lower T_c^-). Such an angle also increases T_a^-, which is the energy that will stay in the system after topology transition.

The mass distribution of the walker (parameterized with μ) has different consequences depending on the torso angle. It can be seen that for negative q_5 a low value μ is better to reduce energy losses, whereas for positive q_5 a high value of μ works better in terms of energetic efficiency. In general, it is better to synthesize gaits with the torso leaning forward ($q_5 > 0°$), and to design robots with the mass more concentrated in the upper body than in the legs ($\mu > 1$) to obtain less consuming heel strike transitions. As before, comparing Figs. 4 and 5 the magnitude of the contact impulses is completely correlated with T_c^-. Therefore, the last considerations given to reduce energy losses also hold if we want to obtain lower impulses.

5. Non-ideal Constraint Realization

If we consider non-ideal inert constraints, then $\bar{\mathbf{f}}_N$ does not disappear in Eq. (10). However, the kinetic energy decomposition expressed in Eq. (7) holds in the same form. The impulses of the generalized non-ideal forces can usually be expressed with force laws such as $\bar{\mathbf{f}}_N = \bar{\mathbf{f}}_N(\bar{\boldsymbol{\lambda}}, \dot{\mathbf{q}}, \mathbf{q})$. They can then be projected to the subspaces and included in the impulsive dynamic equations of the SCM and SAM as $\mathbf{P}_c^T\bar{\mathbf{f}}_N$ and $\mathbf{P}_a^T\bar{\mathbf{f}}_N$, respectively. It can also be shown that for the SCM the associated generalized impulse component can be expressed as $\mathbf{P}_c^T\bar{\mathbf{f}}_N = \mathbf{A}^T\bar{\boldsymbol{\Lambda}}$, where $\bar{\boldsymbol{\Lambda}} = \bar{\boldsymbol{\Lambda}}(\bar{\boldsymbol{\lambda}}, \dot{\mathbf{q}}, \mathbf{q})$ is an $m \times 1$ dimensional array giving the local parameterization of the non-ideal forces in the SCM [9].

With these considerations the impulsive dynamics equations of the SCM and SAM, Eqs. (12) and (13), can be rewritten as

$$\left[\frac{\partial T_c}{\partial \mathbf{v}_c}\right]_-^+ = \mathbf{M}\left(\mathbf{v}_c^+ - \mathbf{v}_c^-\right) = \mathbf{A}^T(\bar{\boldsymbol{\lambda}} + \bar{\boldsymbol{\Lambda}}), \tag{18}$$

$$\left[\frac{\partial T_a}{\partial \mathbf{v}_a}\right]_-^+ = \mathbf{M}\left(\mathbf{v}_a^+ - \mathbf{v}_a^-\right) = \mathbf{P}_a^T\bar{\mathbf{f}}_N. \tag{19}$$

Based on them and Eqs. (3) and (6), we can again write that $\mathbf{v}_c^+ = \mathbf{0}$. And, therefore, using Eq. (18) we obtain that

$$-\mathbf{M}\mathbf{v}_c^- = \mathbf{A}^T(\bar{\boldsymbol{\lambda}} + \bar{\boldsymbol{\Lambda}}), \tag{20}$$

where we need to consider that $\bar{\boldsymbol{\Lambda}}$ can generally be expressed as a function of $\bar{\boldsymbol{\lambda}}$, therefore, this constraint dynamics equation should be solved for $\bar{\boldsymbol{\lambda}}$, which may then be used to evaluate $\bar{\mathbf{f}}_N$. This is needed for the admissible motion dynamics described by Eq. (19). As we did before, based on Eqs. (6), (7) and (20) it is also possible to write that

$$-(\dot{\mathbf{q}}^-)^T\mathbf{M}\mathbf{v}_c^- = -2T_c^- = (\dot{\mathbf{q}}^-)^T\mathbf{A}^T(\bar{\boldsymbol{\lambda}} + \bar{\boldsymbol{\Lambda}}), \tag{21}$$

which shows that even for the case of non-ideal constraint realization, the impulse of the generalized forces developed due to the imposition of the constraints is proportional to the pre-event kinetic energy of the SCM, T_c^-, which is completely lost since $\mathbf{v}_c^+ = \mathbf{0}$. From Eq. (19) it can be seen that the expressions $\dot{\mathbf{q}}^+ = \mathbf{v}_a^+ = \mathbf{v}_a^-$ and $T^+ = T_a^+ = T_a^-$ will not hold for the case of non-ideal impulsive constraints. The kinetic energy of admissible motion T_a will also change during transition as a result of the inert constraints.

6. Example 2: Experimental Analysis of Impact

An experimental testbed based on two dual-pantograph devices has been used to investigate the presented concepts, Fig. 6. Each device is equipped with high-resolution force/torque sensors at the tip and optical encoders at the motor joints. For this study, one of these devices (passive device) emulates a stiff environment with a flat surface and the other (active device) comes to a contact interaction with the passive one at one single contact point. An interface with a conical shape is mounted onto the end effector of the active device to ensure point contact with the flat end plate of the passive system. The compression phase of this interaction represents a topology transition that can be modeled with inert constraints.

Although a single device can move the end effector with the 6-DOF of general 3D motion, the trajectories performed have been programmed so that the motion of the system can be considered planar. The planes of the two pantographs are parallel so they can be considered with one single "composite" pantograph model, see Fig. 7. In this figure, angles q_i denote the absolute orientation of the ith link ($i = 1, 2, 3, 4$) of the pantograph. Regarding the parameters, l_i and a_i represent the length and the position of the center of mass of the ith link, m_i and I_i denote its mass and moment of inertia about its center of mass, and m_{EE} denotes the mass of the end effector. Parameter l_5 indicates the distance between the two actuation motors. The value of these parameters can be found in Table II.

For planar motion, the system can be considered as a 2-DOF mechanism and the actuated joint coordinates $\mathbf{q} = [q_1 \ q_3]^T$ and their time derivatives $\dot{\mathbf{q}}$ may be used as independent generalized coordinates and velocities, respectively. Using this

TABLE II
PARAMETERS OF THE PANTOGRAPH

Parameter	Value	Description
l_1, l_3	0.1449 m	Length of links 1 and 3
l_2, l_4	0.1984 m	Length of links 2 and 4
a_1, a_3	0.0519 m	Position of the COM of links 1 and 3
a_2, a_4	0.1081 m	Position of the COM of links 2 and 4
l_5	0.0445 m	Distance between axes of actuated joints
m_1, m_3	0.1202 kg	Mass of links 1 and 3
m_2, m_4	0.1084 kg	Mass of links 2 and 4
m_{EE}	0.3144 kg	Mass of the end effector
I_1, I_3	0.0004 kgm^2	Moment of inertia of links 1 and 3
I_2, I_4	0.0007 kgm^2	Moment of inertia of links 2 and 4

representation, the mass matrix $\mathbf{M}$ and the Jacobian $\mathbf{A}$ have been determined. Since in the experiments the flat end plate of the passive device has a normal parallel to the y axis, the topology transition can be represented with one inert constraint that describes the sudden imposition of the physical contact constraint on the end point velocity of the active device along the y direction. Therefore, $\dot{y}_{EE}^+ \equiv \mathbf{A}\dot{\mathbf{q}}^+ = 0$.

We have developed experiments to test the influence of the system configuration and velocities on the dynamics of the topology transition. Two different configurations have been studied which are shown in Fig. 8. These will be termed "symmetric configuration" and "asymmetric configuration", according to the figure. For each case, different situations have been tested by varying the angle γ of the pre-event velocity vector of the end effector, $\mathbf{v}_{EE}^- = \begin{bmatrix}\dot{x}_{EE}^- & \dot{y}_{EE}^-\end{bmatrix}^T$, with respect to the direction normal to the contact plane.

An interesting measure that will be used in next sections is the ratio ξ between the pre-event kinetic energy associated with the SCM (which is lost) and the total pre-event kinetic energy of the system. This can be expressed as

$$\xi = \frac{T_c^-}{T^-} = \frac{(\dot{\mathbf{q}}^-)^T \mathbf{P}_c^T \mathbf{M} \mathbf{P}_c \dot{\mathbf{q}}^-}{(\dot{\mathbf{q}}^-)^T \mathbf{M} \dot{\mathbf{q}}^-}, \tag{22}$$

and gives information on what part of the initial kinetic energy is required to develop the constraints. ξ has two extreme values (0 and 1) which are associated with different directions of the tangent space of the system. These directions can be obtained via the formulation of an eigenvalue problem [18].

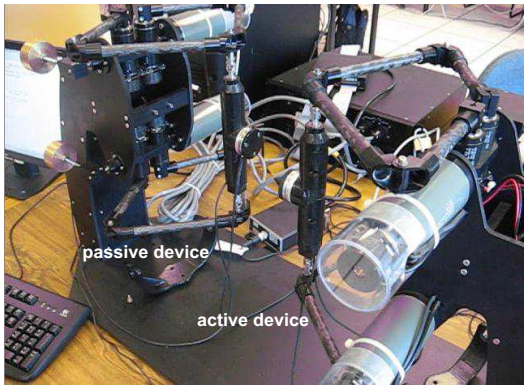

Fig. 6. Experimental setup using two dual-pantograph devices

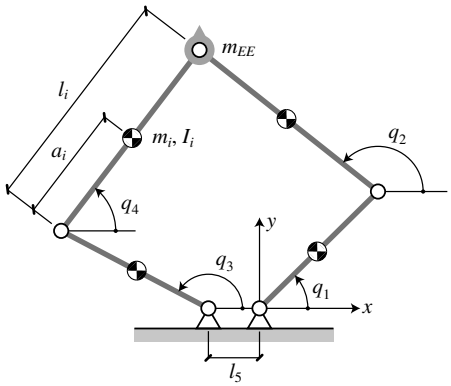

Fig. 7. Planar dynamic model of the pantograph

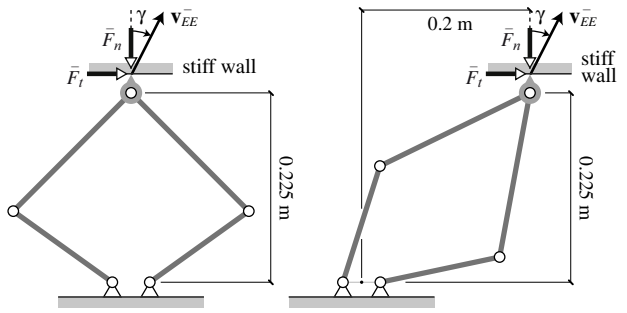

Fig. 8. Contact configurations considered in the experiments

6.1. Results for Symmetric Configuration

For the configuration shown in Fig. 8.a we have performed four sets of experiments where the end point of the active device impacts the flat end plate of the passive one with different velocities (cases **1** to **4**). These are shown in Table III, where γ denotes the angle of the pre-event end point velocity. The magnitudes of these velocity vectors have been determined such that the total pre-event kinetic energy of the system is the same for each case, $T^- = 0.01\,\text{J}$. The table also shows the expected T_c^-, T_a^-, and $\xi = T_c^-/T^-$. As it can be seen $\gamma = 0°$ corresponds to $\xi = 1$, i.e., the situation for which all the pre-impact kinetic energy is associated with the SCM.

For each pre-event velocity, the experiment has been performed several times and the measured results averaged. Fig. 9 shows the results of the kinetic energy decomposition (T_c and T_a) for one individual impact corresponding to each case. The white spots in the plots indicate the values of T_c and T_a at t_i^- (just before contact) and t_i^+ (end of compression). Note that the obtained value of T_c at t_i^+ is zero in all cases, this represents the instant when the inert constraint is established.

Table IV shows the results for the important quantities based on the four sets of experiments, i.e., the kinetic energy decomposition, the ratio ξ, and the measured impulses $\bar{F}_n$ and $\bar{F}_t$ at the tip of the active device (the impulses are defined positive with the sense indicated in Fig. 8). The impulses are determined by numerical integration of the force measurements over the impact interval. Impulse $\bar{F}_n$ is associated with the inert constraint, whereas $\bar{F}_t$ appears due to non-ideal effects, such as friction, along the tangential direction.

It can be first observed that the results in Table IV are in very good agreement with the analytical and computational predictions of Table III, considering that some uncertainties are always present in experimental settings (e.g., in parameter values). It can also be seen that there is a clear correlation between the magnitude of the constraint impulse $\bar{F}_n$ and that of T_c^-. The maximum impulse is obtained for case **1** when all the pre-impact kinetic energy is associated with the SCM, i.e., when $\xi = 1$. It can be seen that T_a changes its value between time points t_i^- and t_i^+ because the tangential impulse $\bar{F}_t$ affects the dynamics of the SAM. However, one can notice that T_a is much less affected than T_c by the topology transition. Note that the change in T_a is related to the magnitude of $\bar{F}_t$.

For case **1** the tangential impulse is low and, therefore, the value of T_a is almost unchanged during topology transition. This can be observed in the top-left plot of Fig. 9. In this case, the tip of the active device has no tangential component of velocity at time t_i^- (since $\gamma = 0°$) and low frictional effects appear during compression. For cases **2** to **4**, tangential impulses are larger because the velocity of the tip at the instant of impact t_i^- has tangential component and, therefore, frictional forces appear during the contact onset. In fact, in these cases $\dot{x}_{EE}^- > 0$ and, since friction forces are opposed to the slipping velocity, this yields negative tangential impulses.

TABLE III
COMPUTATIONS FOR THE FOUR CONSIDERED VELOCITIES

Case	γ	$\|\mathbf{v}_{EE}^-\|$ (m/s)	T_c^- (mJ)	T_a^- (mJ)	ξ
1	0°	0.1974	10	0	1
2	15°	0.1975	9.34	0.66	0.93
3	30°	0.1978	7.53	2.47	0.75
4	45°	0.1981	5.03	4.97	0.50

TABLE IV
EXPERIMENTAL RESULTS FOR THE FOUR CASES (**1**-**4**)

	T_c^- (mJ)	T_a^- (mJ)	T_a^+ (mJ)	ξ	$\bar{F}_n$ (N·ms)	$\bar{F}_t$ (N·ms)
1	9.844	0.010	0.012	1.00	120.53	0.61
2	9.374	0.706	0.519	0.93	107.85	-2.07
3	7.553	2.621	1.987	0.74	101.95	-4.26
4	5.026	5.270	4.443	0.49	82.00	-5.47

6.2. Results for Asymmetric Configuration

We have performed five sets of experiments for the asymmetric configuration shown in Fig. 8.b (cases **5** to **9**). The velocities and expected values of T_c^-, T_a^-, and ξ are shown in Table V. The magnitudes of the velocities have been determined imposing that $T^- = 0.01\,\text{J}$. As before, each experiment has been performed several times and the results averaged. The results for the kinetic energy decomposition during one individual impact are shown in Fig. 10.

It must be noted that for this "asymmetric" configuration $\xi = 1$ does not correspond to an impact with the velocity of the tip aligned with the constrained direction. Using the technique reported in [18], it is obtained that for this configuration $\xi = 1$ (i.e., $T^- = T_c^-$) is achieved when the end point velocity vector $\mathbf{v}_{EE}^-$ forms an angle $\gamma = -7.58°$ with respect to the constrained direction. Since this angle is interpreted positive as shown in Fig. 8, the negative sign means that it

TABLE V
COMPUTATIONS FOR THE FIVE CONSIDERED VELOCITIES

Case	γ	$\|\mathbf{v}_{EE}^-\|$ (m/s)	T_c^- (mJ)	T_a^- (mJ)	ξ
5	−7.58°	0.1955	10	0	1
6	0°	0.1921	9.82	0.18	0.98
7	15°	0.1857	8.57	1.43	0.86
8	30°	0.1812	6.56	3.44	0.66
9	45°	0.1794	4.28	5.72	0.43

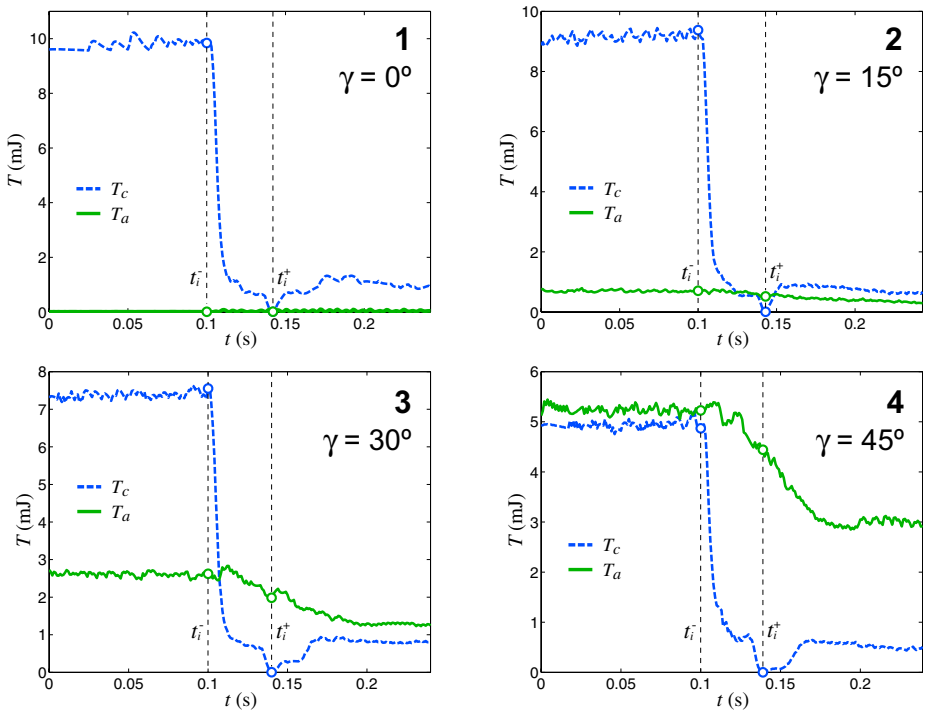

Fig. 9. Kinetic energy decomposition T_c, T_a during one individual experiment for cases **1**-**4** (symmetric configuration)

is measured counterclockwise. The other cases correspond to impact velocities with the same angles γ considered before.

Table VI shows the actual measured quantities of the kinetic energy decomposition, the ratio ξ, and the measured impulses $\bar{F}_n$ and $\bar{F}_t$. These results are in very good agreement with the previous computations in Table V. Several conclusions can be drawn from them. First of all, we find that the maximum constraint impulse is observed for the case of maximum ratio ξ (case **5**). Hence, T_c^- is a good indicator of the magnitude of the constraint forces generated during the transition. As it can be observed, there is a clear correlation between T_c^- and $\bar{F}_n$. This is theoretically supported by Eq. (21).

We believe that this result is not obvious at all. Without performing any analysis one might expect the most intense contact impulses when the end point velocity is fully aligned with the constrained direction ($\gamma = 0°$). However, we have shown here that this is not generally true in complex multibody systems such as the one considered in this work. It can also be noticed that in general $T_a^+ \neq T_a^-$ due to non-ideal phenomena (e.g., friction) represented by impulse $\bar{F}_t$. Note that the largest change in T_a is obtained for case **9** which is the one with the highest tangential impulse. This change can be observed in the corresponding plot of Fig. 10. In cases **5** to **7** the change in T_a is smaller due to lower impulses in the tangential direction.

TABLE VI
EXPERIMENTAL RESULTS FOR THE FIVE CASES (**5**-**9**)

	T_c^- (mJ)	T_a^- (mJ)	T_a^+ (mJ)	ξ	$\bar{F}_n$ (N·ms)	$\bar{F}_t$ (N·ms)
5	9.937	0.001	0.006	1.00	109.57	1.28
6	9.482	0.273	0.223	0.97	105.93	1.40
7	8.506	1.498	1.462	0.85	101.26	0.05
8	6.531	3.490	3.017	0.65	84.97	-2.10
9	4.472	5.693	4.949	0.44	65.17	-2.60

We will discuss now the sign of impulse $\bar{F}_t$. The positive sign for case **5** can be explained because at pre-impact time $\dot{x}_{EE}^- < 0$ (since $\gamma < 0°$) and, therefore, frictional effects are mostly in the opposite sense. Case **6** is not that obvious since for this case we have that $\dot{x}_{EE}^- = 0$, however, the fact that $\bar{F}_t = 1.40$ N·ms implies that there is slipping towards the negative direction of the x axis during the contact onset. In case **7**, the measured tangential impulse is positive and almost zero. One could expect a negative value of such impulse because $\dot{x}_{EE}^- > 0$, however, the measured value implies that slip reversal takes place during interval $[t_i^-,\ t_i^+]$. For cases **8** and **9**, the tangential impulse takes the expected negative sign.

Finally, it must be mentioned that the way kinetic energy is distributed between the SCM and the SAM (before the impact) depends not only on the orientation of the end point velocity relative to the constrained direction, but also on the system configuration at topology change. As it can be observed in Figs. 9 (symmetric configuration) and 10 (asymmetric configuration), the ratio between T_c^- and T_a^- for a given value of γ varies depending on the configuration of the system.

7. CONCLUSION

In this paper we developed a method for the dynamic analysis of variable topology mechanical systems based on the concept of bilateral impulsive constraints. The Jacobian of these constraints can be used to define subspaces of the tangent space of the system, which are termed "space of constrained

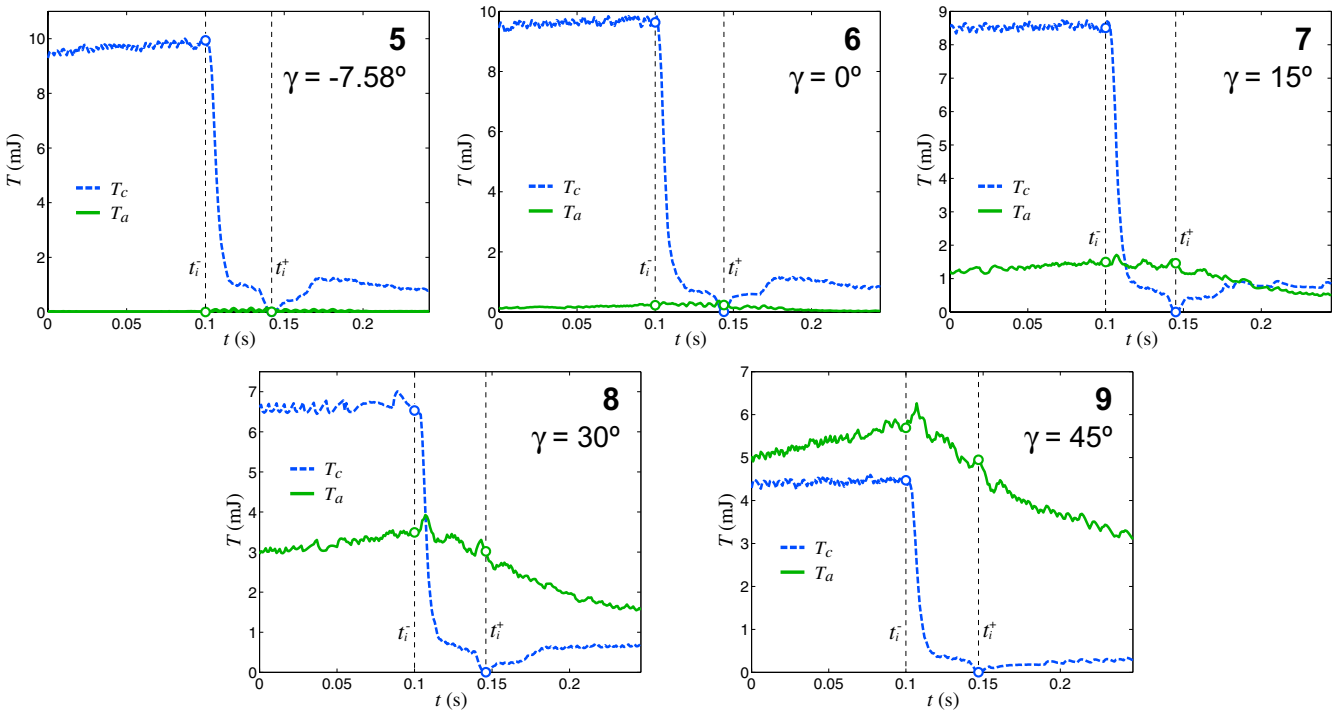

Fig. 10. Kinetic energy decomposition T_c, T_a during one individual experiment for cases **5**-**9** (asymmetric configuration)

motion" and "space of admissible motion". Based on this concept, we completely decoupled the kinetic energy of the system and the impulsive dynamic equations characterizing the event of topology transition. We showed that the pre-event decomposition of the kinetic energy gives useful information on how energy will be redistributed to establish the constraints. We also showed that the energy content in the space of constrained motion has a correlation with the magnitude of the contact impulses generated, both for the case of ideal or non-ideal constraints.

To illustrate the usefulness of the presented concepts two situations that may be characterized with impulsive constraints of that class were studied. First, we analyzed the dynamics of the heel strike event in bipedal locomotion. The kinetic energy redistribution and the impulses on the foot generated during such event were obtained as functions of design parameters and the biped configuration. The analysis carried out provided results that can be useful for control and design of biped robots. We also performed a thorough experimental study of impact using an instrumented robotic testbed. Detailed experimental results that validate the concepts derived from the presented approach are reported.

REFERENCES

[1] K. H. Hwang and A. A. Shabana, "Effect of mass capture on the propagation of transverse waves in rotating beams," *Sound Vib*, vol. 186, no. 33, pp. 495–525, 1995.

[2] G. R. Heppler, "On the dynamic mass capture by flexible robots," in *Control of Flexible Structures*, A. K. Morris, Ed. Providence, RI, USA: American Mathematical Society, 1993, pp. 157–177.

[3] S. H. Collins, A. Ruina, R. Tedrake and M. Wisse, "Efficient bipedal robots based on passive-dynamic walkers," *Science*, vol. 307, pp. 1082–1085, 2005.

[4] T. McGeer, "Passive dynamic walking," *Int J Robot Res*, vol. 9, no. 2, pp. 62–82, 1990.

[5] A. D. Kuo, "Energetics of actively powered locomotion using the simplest walking model," *J Biomech Eng-T ASME*, vol. 124, pp. 113–120, 2002.

[6] L. A. Pars, *A Treatise on Analytical Dynamics*. London, England, UK: Heinemann, 1965.

[7] F. Pfeiffer, "Mechanische Systeme mit Unstetigen Übergängen," *Ing Arch*, vol. 54, pp. 232–240, 1984.

[8] J. Kövecses and W. L. Cleghorn, "Finite and impulsive motion of constrained mechanical systems via jourdain's principle: Discrete and hybrid parameter models," *Int J Nonlinear Mech*, vol. 38, pp. 935–956, 2003.

[9] J. Kövecses, "Dynamics of mechanical systems and the generalized free-body diagram - Part I: General formulation," *J Appl Mech-T ASME*, vol. 75, 061012, pp. 1–12, 2008.

[10] W. Blajer, "A geometric unification of constrained system dynamics," *Multibody Syst Dyn*, vol. 7, no. 1, pp. 3–21, 1997.

[11] J. Kövecses, J. C. Piedbœuf and C. Lange, "Dynamics modeling and simulation of constrained mechanical systems," *IEEE-ASME T Mech*, vol. 8, no. 2, pp. 165–177, 2003.

[12] S. A. Modarres Najafabadi, "Dynamics modelling and analysis of impact in multibody systems," Ph.D. dissertation, Department of Mechanical Engineering, McGill University, Montréal, Québec, Canada, 2008.

[13] L. Y. Bahar, "On the use of quasi-velocities in impulsive motion," *Int J Eng Sci*, vol. 32, no. 11, pp. 1669–1686, 1994.

[14] F. Asano and Z. W. Luo, "Asymptotically stable gait generation for biped robot based on mechanical energy balance," in *Proc IEEE Conf Int Robots and Systems*, San Diego, CA, USA, 2007, pp. 3327–3333.

[15] F. Asano, Z. W. Luo and M. Yamakita, "Biped gait generation and control based on a unified property of passive dynamic walking," *IEEE T Robot*, vol. 21, no. 4, pp. 754–762, 2005.

[16] M. Kwan and M. Hubbard, "Optimal foot shape for a passive dynamic biped," *J Theor Biol*, vol. 248, no. 2, pp. 331–339, 2007.

[17] F. Asano and Z. W. Luo, "The effect of semicircular feet on energy dissipation by heel-strike in dynamic biped locomotion," in *Proc IEEE Conf Robotics and Automation*, Rome, Italy, 2007, pp. 3976–3981.

[18] J. Kövecses and J. M. Font-Llagunes, "An eigenvalue problem for the analysis of variable topology mechanical systems," *J Computational Nonlinear Dynamics-T ASME*, 2009, to appear.